metals

MDPI

Article

An Investigation of Atomic Interaction between Ag and Ti_2AlC under the Processing Temperature of 1080 °C

Guochao Wang [1,†], Yafei Li [2,†], Weijian Chen [2], Jianguo Yang [2], Jie Zhang [3,*] and Yanming He [2,*]

[1] 38th Research Institute, China Electronics Technology Group Corporation, Hefei 230000, China; wangguoc@cetc38.com.cn
[2] Institute of Process Equipment and Control Engineering, Zhejiang University of Technology, Hangzhou 310014, China; lyf@zjut.edu.cn (Y.L.); weijianchen@zjut.edu.cn (W.C.); yangjg@zjut.edu.cn (J.Y.)
[3] School of Materials Science and Engineering, Harbin Institute of Technology, Harbin 150001, China
* Correspondence: hitzhangjie@hit.edu.cn (J.Z.); heyanming@zjut.edu.cn (Y.H.)
† These authors contributed equally to this work.

Abstract: Ti_2AlC is a typical MAX (M: early transition metal, A: main group element, and X: carbon and/or nitrogen) phase with ceramic and metallic properties due to its unique nano-layered structure. In order to investigate the interaction behavior between Ag and Ti_2AlC, a sessile drop experiment was conducted at 1080 °C for 5 min. The atomic rearrangement occurred at the Ag–Ti_2AlC interface was revealed using high-angle annular dark-field scanning transmission electron microscopy coupled with high-resolution transmission electron microscopy analysis. The results show that Ag nanoclusters generally appeared in most of the Ag–Ti_2AlC interaction regions thermally processed at 1080 °C. In addition, Ag can also substitute for Al and Ti atoms in the Ti_2AlC, promoting local structural decomposition of the Ti_2AlC and producing 4H–Ag with a hexagonal close-packed (hcp) structure. Additionally, Al atoms released from the Ti_2AlC lattices can dissolve locally into the liquid Ag, particularly at the grain boundaries. When the loss concentration of Al exceeded the critical level, the Ti_2AlC started to decompose and the residual Ti_6C octahedrons and Al atoms recombined, giving rise to the production of anti-perovskite Ti_3AlC with a cubic structure. Lastly, the discrepancy in substitution behavior of Ag in the Ti_2AlC was compared when thermally processed at different temperatures (1030 °C and 1080 °C). This work contributes to the understanding of the intrinsic stability of Ti_2AlC MAX ceramics under high-temperature treatment.

Keywords: Ag–Ti_2AlC system; sessile drop experiment; high-temperature interaction; atomic rearrangement

Citation: Wang, G.; Li, Y.; Chen, W.; Yang, J.; Zhang, J.; He, Y. An Investigation of Atomic Interaction between Ag and Ti_2AlC under the Processing Temperature of 1080 °C. *Metals* **2021**, *11*, 1963. https://doi.org/10.3390/met11121963

Academic Editors: Donatella Giuranno, Fabrizio Valenza and Martin Bache

Received: 21 October 2021
Accepted: 3 December 2021
Published: 6 December 2021

1. Introduction

Ti_2AlC ceramics, as a representative 211-type MAX phase, have attracted increased attention recently [1–3]. The unique nano-layered structure and diverse bonding characteristics enable them to possess both ceramic and metallic properties [4–6]. However, studies on Ti_2AlC ceramics are relatively few, which limits the understanding toward their intrinsic properties and structural characteristics. Among the MAX-phase materials, Ti_2AlC has a low density (4.11 $g \cdot cm^{-3}$) [7], high thermal conductivity (46 $W/m \cdot K$) [8], and excellent electrical conductivity (4.42 $\times$ 10^6 $S \cdot m^{-1}$) [9]. In particular, the ceramic has a coefficient of thermal expansion of 8.8 $\times$ 10^6 $°C^{-1}$, which means that it exhibits outstanding high-temperature oxidation resistance [10,11]. Based on this, Ti_2AlC will be expected to be used in applications with frequent alternation of thermal cycles, such as the heating bodies of furnaces [12], coating materials of atomic energy reactors [13,14], and current-carrying friction devices [15,16]. However, it is difficult to prepare pure Ti_2AlC with a large size and complex shape because its compositional range is rather narrow [17]. The joining of the Ti_2AlC to itself or to metals, as well as dissimilar materials, will enable the production and assembly of components with complex shapes and will also improve

the capabilities and properties of such materials. For example, heat sink components, automotive commutators, and electric locomotive pantograph pans require the joining of C-based materials (such as graphite) with Cu [18–20]. Compared with C-based materials, Ti_2AlC has greater strength, better high-temperature stability, self-lubrication capability, and better conductivity [21]. Replacement of the C-based materials with the Ti_2AlC will enhance the component performance and extend the service life.

Brazing is commonly used to join non-metallic materials to metallic materials [22,23]. The design and selection of brazing filler materials are very important, and are directly related to the joining quality. Generally, Ag and Cu based brazing filler alloys are commonly used for joining ceramics [24,25]. Considering the fact that the elements in the brazing filler materials will interact with substrates, it is critical to understand their interaction behavior during brazing. The Ag–Cu brazing filler alloys have been introduced to join Ti_2AlC and Cu, with strong joints being achieved [26,27]. The strong affinity of Cu (from the Ag–Cu filler alloys and Cu substrates) toward Ti and Al (from the Ti_2AlC) gave rise to the formation of $AlCu_2Ti$ in the braze seam, leading to the structural decomposition of Ti_2AlC. The dissolution of Cu substrates beside the braze seam provided sufficient Cu for the reaction. Compared with Cu, the interaction of Ag with Ti_2AlC was relatively weaker at the processing temperature of 1030 °C [28]. Based on these Ag nanoclusters, nanotwins and polycrystals were distributed in the Ti_2AlC lattices after joining. No decomposition of the Ti_2AlC was detected. Unfortunately, the interaction mechanism between Ag and Ti_2AlC under higher temperatures (over 1300 °C) has yet to be reported. An investigation of the interaction of Ag with Ti_2AlC over a wide temperature range could help in screening alloying elements for the design of brazing filler materials, promoting the understanding toward the intrinsic structure, bonding characteristics, and crystal stability of the Ti_2AlC. The basic theory about the atomic-scale structure of Ti_2AlC will, therefore, be enriched, creating a prerequisite condition to promote its engineering applications. For this, the presented work was focused on studying the substitution behavior of Ag in the Ti_2AlC and the structural stability of this kind of ceramic at high temperatures (for example 1080 °C). The sessile drop experiment was performed to investigate the interaction behavior in the Ag–Ti_2AlC system under isothermal conditions at 1080 °C for 5 min and the as-obtained interface was examined by transmission electron microscope (TEM). The spherical aberration-corrected scanning transmission electron microscope analysis was conducted for the TEM foils of the Ag–Ti_2AlC interaction zones.

2. Materials and Methods

The Ti_2AlC ceramics synthesized by self-propagating high-temperature synthesis were purchased from Wuhan University of Technology. They were cut into $3 \times 4 \times 3$ mm^3 samples for microstructural observation. The microstructure of the Ti_2AlC used in the current work is shown in Figure 1a, in which two regions with different contrasts can be distinguished. The energy-dispersive spectroscopy (EDS) analysis indicates that the two regions share a similar composition. The X-ray diffraction (XRD) results for the Ti_2AlC is presented in Figure 1b. It can also be shown from the picture that in addition to the diffraction peaks of the Ti_2AlC, no other diffraction information can be described, suggesting the Ti_2AlC is pure.

The high-temperature interactions between Ag and Ti_2AlC were evaluated by a sessile drop experiment. First, pure Ag powders were placed in the mold and then they were pressed into cylindrical pellets using a uniaxial two-sided compaction method. Next, the cylindrical Ag pellet was placed on the surface of the Ti_2AlC and put into a vacuum furnace. The contact angle value measurement instrument coupled with the vacuum furnace was introduced to inspect the contact angle during the heating stage. The highest temperature was 1080 °C and isothermal soaking was performed for 5 min. During heating, the samples were first heated up to 900 °C with a heating rate of 20 °C/min and held for 10 min to achieve temperature homogenization. The Ag pellet still preserved a cylindrical shape at 900 °C, since the melting point of Ag (~961 °C) had not been reached, as shown in

Figure 2b. The temperature was increased up to 1080 °C at a rate of 5 °C/min. The Ag pellet started to melt and spread out to form a spherical droplet, as described in Figure 2c. The wetting angle was found to be 21°, suggesting very good wetting at the Ag–Ti_2AlC triple line. After heating, the samples were cooled to room temperature. In order to conduct the TEM examination, the middle part of the sample was cross-cut to expose interaction zones. A wafer with a diameter of ~3 mm was then machined from the interaction zones. The thickness of the wafer was mechanically polished to 40 μm, followed by ion milling. It should be noted that the central region of the wafer was polished to nearly 10 μm in thickness, which was achieved using a RES101-type ion-beam thinner (Leica, Wetzlar, Germany) working at 5 kV. Finally, the spherical aberration-corrected transmission electron microscope (ARM200F, JEOL, Tokyo, Japan) equipped with an X-ray spectrometer and a high-angle annular dark-field (HAADF) probe (operating at 200 kV) was performed for the TEM thin foils to reveal atomic-scale information.

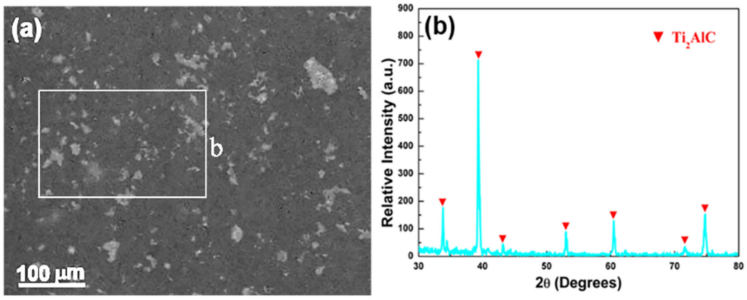

Figure 1. (**a**) SEM back-scattered electron (BSE) image of the Ti_2AlC and (**b**) corresponding XRD (X-ray diffraction) result.

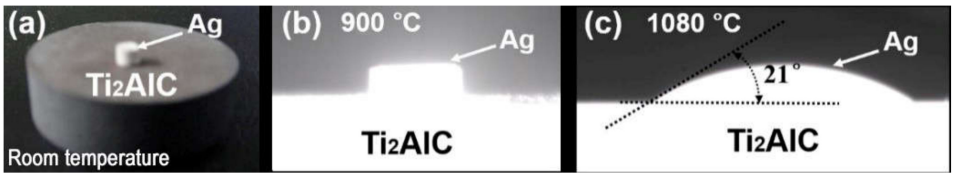

Figure 2. Wetting experiment of Ag on the Ti_2AlC conducted at 1080 °C for 5 min using the sessile drop method: (**a**) before wetting; (**b**) 900 °C; (**c**) 1080 °C.

3. Results and Discussion

3.1. Phenomenon 1: Structural Transformation of Ag in the Ti_2AlC

Figure 3a shows the HAADF–STEM (High-angle Annular Dark-field Scanning Transmission Electron Microscopy) morphology of the Ag–Ti_2AlC interaction zone along with the crystallographic orientation of $[11\bar{2}0]_{Ti_2AlC}$. Apart from the Ag nanoclusters, another atomic arrangement can also be revealed from the figure. This zone measures ~40 × 100 nm, which is much larger than the critical size of Ag nanoclusters (9.072 nm) in the Ti_2AlC [28]. The boundary of this zone is parallel to basal plane of the Ti_2AlC. The magnified rectangular box in Figure 3a is indicated in Figure 3b, which exhibits two representative atomic arrangements. The upper part in Figure 3b shows the atomic arrangement of Ag under the zone axis of $[\bar{1}101]_{Ag}$, while the lower part exhibits the atomic arrangement of Ti_2AlC under the zone axis of $[11\bar{2}0]_{Ti_2AlC}$, in which a parallel relationship can be found between them. Figure 3c,d presents their fast Fourier transformation (FFT) results. It has been mentioned that Ag occurred in the Ti_2AlC in the form of nanoclusters, nanotwins, or polycrystals under a lower processing temperature of 1030 °C [28]. In the current work, Ag with a hexagonal close-packed (hcp) structure was first detected in the Ti_2AlC. Similar to the Ti_2AlC, the 4H–Ag (ICDD PDF #01-087-0598) [29] with the hcp structure has a space group of *P63/mmc* through measuring the interplanar spacing. It can be seen from Figure 3f that both the 4H–Ag and Ti_2AlC share a similar long-periodic crystal structure, differing in the length of *c*-axis slightly. It is also demonstrated in Figure 3b that the crystal lattice of

Ag is parallel to that of the Ti_2AlC in one direction. Figure 3e presents the FFT results of the interaction zone in Figure 3b. A specific crystallographic relationship can be derived between the 4H–Ag and Ti_2AlC:

$$[\bar{1}101]_{Ag} \,||\, [11\bar{2}0]_{Ti_2AlC} \quad (1)$$

$$(1\bar{1}02)_{Ag}||(0002)_{Ti_2AlC} \quad (2)$$

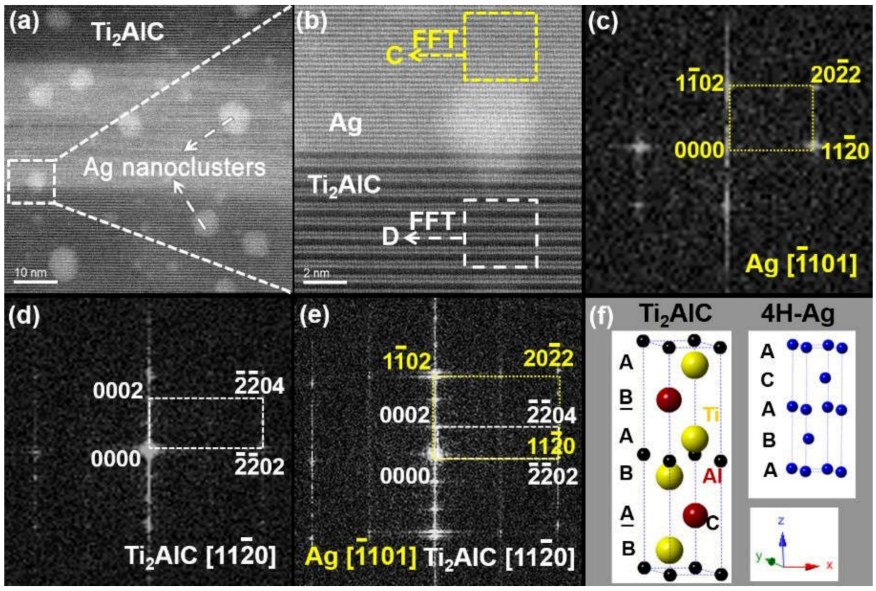

Figure 3. TEM results of the Ag–Ti_2AlC interaction zone along the crystallographic orientation of $[11\bar{2}0]_{Ti_2AlC}$: (**a**) HAADF–STEM image; (**b**) magnified white box in (**a**); (**c**,**d**) FFT (fast Fourier transformation) results of the Ag and Ti_2AlC in (**b**); (**e**) FFT result of the Ag–Ti_2AlC interface in (**b**); (**f**) schematic drawings of the crystal structures of 4H–Ag and Ti_2AlC.

It has been reported that Al atoms can separate from the Ti_2AlC lattices and migrate along the crystallographic plane of (0001) under high temperature (for example 1080 °C), producing vacancies and diffusion channels [30–33]. Coupled with the outward migration of Al atoms, Ti atoms would also break away from the Ti_2AlC and likewise give rise to the vacancies. However, the Ti_2AlC still preserved its normal crystal structure despite losing parts of Al and Ti atoms. The Ag atoms entered into the Ti_2AlC lattices along the diffusion channels and occupied part of the vacancies. The occupation of Al vacancies by Ag was beneficial in reducing the vacancy formation energy of Al, which means that the substitution behavior of Ag promoted the generation of more Al vacancies in the Ti_2AlC. To maintain integrity, the Ti_2AlC could withstand vacancy concentrations of up to 50% [34,35], far greater than the limit of the Ag concentration replacing Al (~12.5%). It can be speculated that redundant vacancies would be filled by Ag atoms when the vacancy concentration of Al is greater than the substitution ratio of Ag. Upon cooling from 1080 °C, Ag nucleated and grew up epitaxially along the basal planes of the Ti_2AlC (namely atomic-diffusion-driven channels), generating the 4H–Ag with the hcp structure; that is, Ag could replace Al and Ti atoms in the Ti_2AlC. The 4H–Ag was, therefore, precipitated from the Ti_2AlC locally, leading to the instability of the Ti_2AlC.

3.2. Phenomenon 2: Structural Transformation of the Ti_2AlC at the Grain Boundaries

It should be mentioned that no clear crystallographic orientation relationship between the Ag and Ti_2AlC was inspected for most of the interaction zones thermally processed at 1080 °C for 5 min. However, a specific crystallographic relationship can still be detected locally. Figure 4 indicates the TEM results of the Ag and Ti_2AlC at the grain boundaries. It can be seen from Figure 4a that the white phase belongs to the Ag, while the gray

phase is actually the Ti_2AlC. The yellow box in Figure 4a shows the morphology of the Ag–Ti_2AlC interface, with a high-resolution TEM image presented in Figure 4b. Figure 4c,d describes the FFT results of the two phases in shown in Figure 4b. It can be demonstrated from Figure 4c that Ag in Figure 4a has a cubic structure. Interestingly, the gray phase with a cubic structure does not belong to the Ti_2AlC according to its diffraction pattern in Figure 4d. Based on the structural information, the gray phase may belong to following phases: Ag (Ti, Al), TiC, and Ti_3AlC. It can be excluded that the phase belongs to Ag (Ti, Al) because there is a significant discrepancy in contrast (Figure 4a) between this phase and Ag. Table 1 provides the theoretical and experimental lattice parameters of the three phases. The theoretical values of the lattice parameters were obtained from [36], while the experimental values were calculated from the diffraction patterns in Figures 4 and 5. According to the presented results, the experimental lattice parameters of the gray phase approach the theoretical value of the Ti_3AlC. It can then be inferred that the gray phase in the yellow box (Figure 4a) should be determined to be the Ti_3AlC.

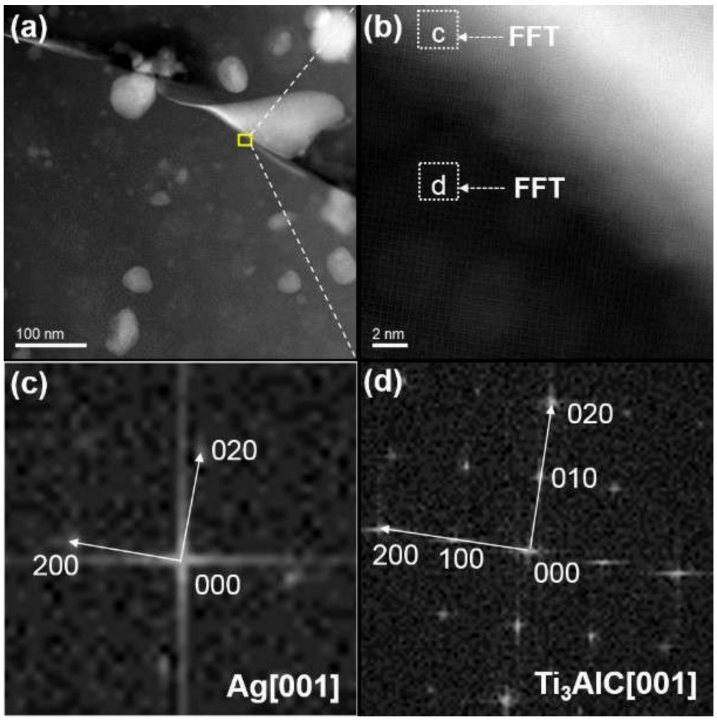

Figure 4. TEM results of the Ag and Ti_2AlC at the grain boundaries: (**a**) HAADF–STEM image; (**b**) high-resolution TEM image of yellow box in (**a**); (**c**,**d**) FFT results of (**b**).

Table 1. Theoretical and experimental lattice parameters of the Ag, TiC, and Ti_3AlC.

Phase	Theoretical Value (Å) [36]		Experimental Value (Å)	
	$d_{\{220\}}$	$d_{\{200\}}$	$d_{\{220\}}$	$d_{\{200\}}$
Ag	1.445	2.044	1.487	2.085
TiC	1.530	2.163	–	–
Ti_3AlC	1.465	2.074	1.438	2.011

Figure 5 describes the detailed TEM results of the Ti_3AlC. It can be seen from Figure 5a that a number of Ag nanoclusters with different sizes are scattered in the Ti_3AlC. Figure 5b shows the atomic arrangement of the white dashed box in shown in Figure 5a. Observing the investigated zone axis, it can be shown that the Ti_3AlC lattices are composed of regular square grids with three atoms at each side and one atom in the center. The FFT in Figure 5b yields the diffraction patterns shown in Figure 5c. In general, diffraction does not occur easily on the crystallographic planes of (010) and (100) under the zone axis of [001] for

the cubic structure. However, for the Ti_3AlC with an anti-perovskite cubic structure, the diffraction could happen at such a position [37–39]. Actually, the anti-perovskite Ti_3AlC belongs to a metallic carbide, as presented in Figure 5d. A single cell contains Ti atoms at the face-centered position, Ag atoms at the corner position, and a C atom at the body-centered position. Compared to the Ti_2AlC, the Ti_3AlC can be described as a Ti_6C octahedron placed in a cubic Al cell. The lattice arrangement of the Ti_3AlC obtained by projection under the zone axis of [001] corresponds to the lattice arrangement in Figure 5b perfectly; that is, the face-centered position in the Ti_3AlC contains Ti atoms, and their projection position is located at the center of the square gird and side length. The vertex position contains Al atoms, corresponding to the vertex position of the square grid in Figure 5b. The body-centered position contains the C atom, while its projection position overlaps the position of the Ti atom at the face-centered position. This demonstrates that the gray phase in the yellow box (Figure 4a) should belong to the Ti_3AlC.

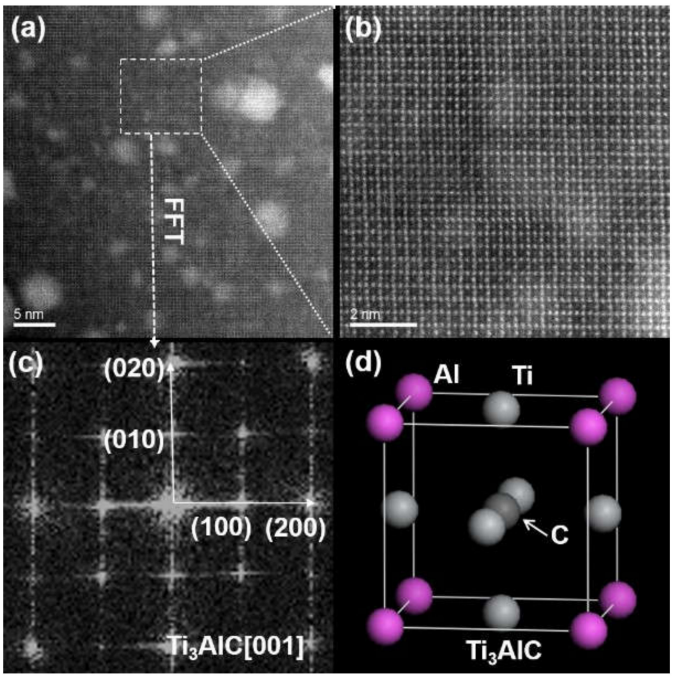

Figure 5. TEM results of the Ti_3AlC: (**a**) high-resolution TEM image of the Ti_3AlC; (**b**) magnified white dashed box shown in (**a**); (**c**) FFT result shown in (**b**); (**d**) crystal structure of the Ti_3AlC.

It has been mentioned in Figure 1 that no Ti_3AlC was observed in the Ti_2AlC substrates. Therefore, the Ti_3AlC (Figures 4 and 5) should be produced through the interaction of Ag with Ti_2AlC during high-temperature treatment. The high-resolution TEM of the Ag–Ti_3AlC interface is shown in Figure 6a and its inverse FFT result is shown in Figure 6b. The Ag and Ti_3AlC can be distinguished from the figure because the size of the Ag lattice is one-quarter of the Ti_3AlC. Despite this, the interface of Ag and Ti_3AlC shares a completely coherent relationship. It can also be detected that a small lattice mismatch occurred at their phase boundaries. This lattice mismatch accumulation resulted in apparent lattice distortion. The lattice-distortion-driven stacking faults can be seen in Figure 6c (magnified white dashed box shown in Figure 6b). The FFT result of Figure 6a is shown in Figure 6d. It is worth noting that only a set of diffraction patterns can be detected, which hints that the diffraction patterns of the Ag and Ti_3AlC should overlap. The overlapping phenomenon arises because they have a similar crystal structure and share a coherent relationship at the interface. Based on this, the crystallographic orientation relationship between the Ag and Ti_3AlC can be described below:

$$(002)_{Ag}//(002)_{Ti_3AlC} \quad (3)$$

$$[001]_{Ag}//[001]_{Ti_3AlC} \quad (4)$$

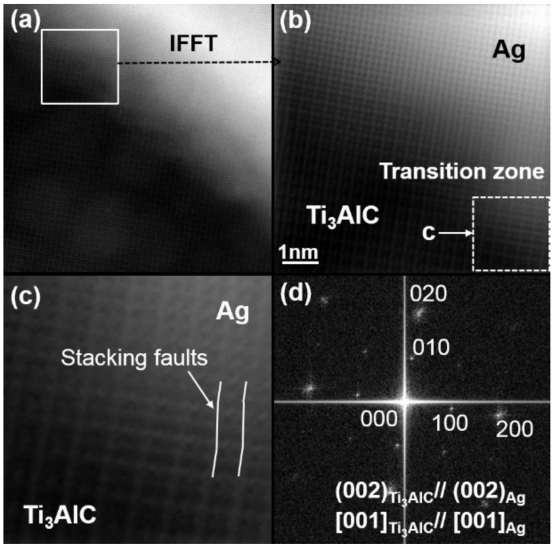

Figure 6. TEM results of the Ag–Ti_3AlC interface: (**a**) high–resolution TEM image; (**b**) magnified white box in shown in (**a**); (**c**) magnified white dashed box shown in (**b**); (**d**) IFFT (inverse fast Fourier transformation) result shown in (**a**).

Figure 7 presents atomic models of the Ag and Ti_3AlC, showing their crystal structure and crystallographic orientation relationship. The lattice of the Ag and Ti_3AlC obtained through projection under the zone axis of [001] is arranged along the crystallographic plane of (001) symmetrically, leading to a coherent relationship. Based on this, the formation mechanism of the Ti_3AlC can be inferred (Figure 8). It is worth noting that the Ti_2AlC lattice was formed through the alternating distribution of Ti–C octahedrons and Al atom layers. When the heating temperature exceeded the melting temperature of Ag (~961 °C), Al separated from the Ti_2AlC and dissolved into the liquid Ag at the grain boundaries. When the loss of Al concentration reached the critical level, Ti_2AlC destabilized, leading to the rearrangement of Ti–C octahedrons and Al atoms. For this, the Ti_2AlC with the hcp structure was transformed into the anti-perovskite Ti_3AlC with a face-centered cubic (fcc) structure locally. The cubic Ag was solidified along the Ti_3AlC epitaxially during cooling and a coherent relationship was shared between them.

The interaction of Ag with Ti_2AlC has been investigated at 1030 °C [28]. It has been reported that Ag atoms can substitute for Al and Ti atoms in the Ti_2AlC. By increasing the amount of Ag, Ag nanoclusters, nanotwins, and polycrystals nucleated and grew up in the Ti_2AlC lattices without destroying the integrity. When the temperature was increased to 1080 °C, Ag generally appeared in the Ti_2AlC in the form of nanoclusters. However, the Ti_2AlC started to decompose locally when the substitution ratio of Ag exceeded the limiting ratio. For example, Ag atoms could replace Al and Ti atoms in the Ti_2AlC, triggering the formation of the 4H–Ag with the hcp structure along the specific crystallographic plane and orientation of the Ti_2AlC. Apart from this, parts of Al atoms could also de-intercalate from the Ti_2AlC lattices at the grain boundaries to promote the transformation from the Ti_2AlC to Ti_3AlC.

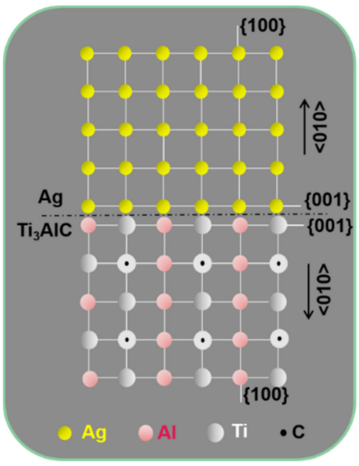

Figure 7. Atomic models showing the crystal structure of the Ag and Ti_3AlC and their crystallographic orientation relationship.

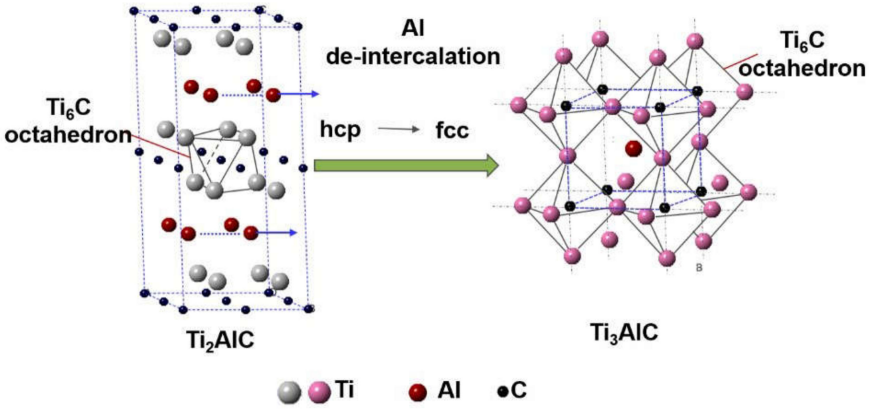

Figure 8. Schematic description of the transformation from the Ti_2AlC to Ti_3AlC. HCP: a hexagonal close-packed. FCC: face-centered cubic.

4. Conclusions

The interaction of Ag with Ti_2AlC was investigated to better understand the basic rule of atomic rearrangement at high temperatures (for example, 1080 °C). The Ag–Ti_2AlC interaction zones were experimentally investigated via the sessile drop experiment conducted under isothermal conditions at T = 1080 °C for 5 min. The substitution behavior of Ag atoms in the Ti_2AlC was investigated using the TEM analysis. Observing along the crystallographic orientation of $[11\bar{2}0]_{Ti_2AlC}$, Ti_2AlC was found to decompose upon in contact with molten Ag. Ag nucleated along the basal plane of Ti_2AlC during cooling and grew into the 4H–Ag with the hcp structure, which shared a specific crystallographic orientation relationship with the original Ti_2AlC. In local regions, particularly at the Ag–Ti_2AlC grain boundaries, parts of Al atoms broke away from the Ti_2AlC lattices, while the Ti_6C octahedrons coupled with the remaining Al–atomic layers gave rise to the generation of the Ti_3AlC. A specific crystallographic orientation relationship was also produced between the Ag and Ti_3AlC. To sum up, Ag appeared in the Ti_2AlC in the form of nanoclusters for most of the Ag–Ti_2AlC interaction zones thermally processed at 1080 °C. When the substitution ratio of Ag far exceeded the limiting ratio, Ti_2AlC was locally decomposed.

Author Contributions: Conceptualization, J.Z. and Y.H.; investigation, G.W. and W.C.; resources, J.Z. and Y.H.; writing—original draft preparation, G.W. and Y.L., writing—review and editing, J.Y. All authors have read and agreed to the published version of the manuscript.

Funding: This research was funded by the Primary Research & Development Plan of Zhejiang Province (Gran no. 2021C01178), National MCF Energy R&D Program (Gran no. 2019YFE03100400), and National Natural Science Foundation of China (grant number 52175368 and 51975530).

Institutional Review Board Statement: Not applicable.

Informed Consent Statement: Not applicable.

Data Availability Statement: The data presented in this study are available on request from the corresponding author.

Conflicts of Interest: There are no conflicts to declare.

References

1. Thomas, T.; Zhang, C.; Sahu, A.; Nautiyal, P.; Loganathan, A.; Laha, T.; Boesl, B.; Agarwal, A. Effect of graphene reinforcement on the mechanical properties of Ti_2AlC ceramic fabricated by spark plasma sintering. *Mater. Sci. Eng. A* **2018**, *728*, 45–53. [CrossRef]
2. Sun, Y.; Zhou, C.; Zhao, Z.; Wu, G. High plasticity achieved by spark plasma sintering method in aluminum matrix composites reinforced with Ti_2AlC particles. *Mater. Charact.* **2021**, *177*, 111204. [CrossRef]
3. Lee, G.W.; Kim, T.W.; Sloof, W.G.; Lee, K.S. Self–healing capacity of Mullite–Yb_2SiO_5 environmental barrier coating material with embedded Ti_2AlC MAX phase particles. *Ceram. Int.* **2021**, *47*, 22478–22486. [CrossRef]
4. Yu, W.; Guénolé, J.; Ghanbaja, J.; Vallet, M.; Guitton, A. Frank partial dislocation in Ti_2AlC–MAX phase induced by matrix–Cu diffusion. *Scripta Mater.* **2021**, *191*, 34–39. [CrossRef]
5. Liu, K.; Li, Y.; Yang, J.; Liu, Y.; Yao, Y. Generative principal component thermography for enhanced defect detection and analysis. *IEEE. Trans. Instrum. Meas.* **2020**, *69*, 8261–8269. [CrossRef]
6. Barsoum, M.W. The $M_{N+1}AX_N$ phases: A new class of solids: Thermodynamically stable nanolaminates. *Prog. Solid. State. Chem.* **2000**, *28*, 201–281. [CrossRef]
7. Li, X.; Xie, X.; Gonzalez-Julian, J.; Malzbender, J.; Yang, R. Mechanical and oxidation behavior of textured Ti_2AlC and Ti_3AlC_2 MAX phase materials. *J. Eur. Ceram. Soc.* **2020**, *40*, 5258–5271. [CrossRef]
8. Barsoum, M.W.; Salama, I.; El-Raghy, T.; Golczewski, J.; Seifert, H.J.; Aldinger, F.; Porter, W.D.; Wang, H. Thermal and electrical properties of Nb_2AlC, $(Ti, Nb)_2AlC$ and Ti_2AlC. *Metall. Mater. Trans. A* **2002**, *33*, 2775–2779. [CrossRef]
9. Fey, T.; Stumpf, M.; Chmielarz, A.; Colombo, P.; Greil, P.; Potoczek, M. Microstructure, thermal conductivity and simulation of elastic modulus of MAX-phase (Ti_2AlC) gel-cast foams. *J. Eur. Ceram. Soc.* **2018**, *38*, 3424–3432. [CrossRef]
10. Lu, J.L.; Abbas, N.; Tang, J.N.; Tang, J.; Zhu, G.M. Synthesis and characterization of conductive ceramic MAX-phase coatings for metal bipolar plates in simulated PEMFC environments. *Corros. Sci.* **2019**, *158*, 108106. [CrossRef]
11. Byeon, J.; Liu, J.; Hopkins, M.; Fischer, W.; Garimella, N.; Park, K.; Brady, M.; Radovic, M.; El-Raghy, T.; Sohn, Y. Microstructure and residual stress of alumina scale formed on Ti_2AlC at high temperature in air. *Oxid. Met.* **2007**, *68*, 97–111. [CrossRef]
12. Wang, Z.; Li, W.; Wang, C.; Wu, H.; Ke, P.; Wang, A. Transforming the amorphous Ti-Al-C coatings to high-purity Ti_2AlC MAX phase coatings by prolonged annealing at 550 °C. *Mater. Lett.* **2020**, *261*, 127160. [CrossRef]
13. Xiao, J.; Yang, T.; Wang, C.; Xue, J.; Wang, Y. Investigations on radiation tolerance of $M_{n+1}AX_n$ phases: Study of Ti_3SiC_2, Ti_3AlC_2, Cr_2AlC, Cr_2GeC, Ti_2AlC, and Ti_2AlN. *J. Am. Ceram. Soc.* **2015**, *98*, 1323–1331. [CrossRef]
14. Mazaheri, Y.; Bahiraei, M.; Jalilvand, M.M.; Ghasemi, S.; Heidarpour, A. Improving mechanical and tribological performances of pure copper matrix surface composites reinforced by Ti_2AlC MAX phase and MoS_2 nanoparticles. *Mater. Chem. Phys.* **2021**, *270*, 124790. [CrossRef]
15. Richardson, P.; Cuskelly, D.; Brandt, M.; Kisi, E. Effects of furnace annealing on in situ reacted Ti_2AlC MAX phase composite coatings deposited by laser cladding. *Surf. Coat. Technol.* **2021**, *405*, 126597. [CrossRef]
16. Ma, Y.; Huang, X.; Hang, W.; Liu, M.; Song, Y.; Yuan, J.; Zhang, T. Nanoindentation size effect on stochastic behavior of incipient plasticity in a $LiTaO_3$ single crystal. *Eng. Fract. Mech.* **2020**, *226*, 106877. [CrossRef]
17. Pietzka, M.; Schuster, J. Summary of constitutional data on the aluminum–carbon–titanium system. *J. Phase. Equilibria* **1994**, *15*, 392–400. [CrossRef]
18. Lin, Y.; Maozhong, Y.; Liping, R. Tribological behavior of a novel C/C–Cu sliding electrical contact material. *Tribology* **2009**, *29*, 458–463. [CrossRef]
19. Zhou, Z.; Zhong, Z.; Qu, D.; Ge, C. Design and joining of graphite to copper by a simple direct casting technology. *Int. J. Mater. Prod. Technol.* **2011**, *42*, 21–28. [CrossRef]
20. Manohar, G.; Pandey, K.M.; Maity, S.R. Effect of microwave sintering on the microstructure and mechanical properties of AA7075/B_4C/ZrC hybrid nano composite fabricated by powder metallurgy techniques. *Ceram. Int.* **2021**, *47*, 32610–32618. [CrossRef]
21. Bentzel, G.W.; Ghidiu, M.; Anasori, B.; Barsoum, M.W. On the interactions of Ti_2AlC, Ti_3AlC_2, Ti_3SiC_2 and Cr_2AlC with silicon carbide and pyrolytic carbon at 1300 degrees C. *J. Eur. Ceram. Soc.* **2015**, *35*, 4107–4114. [CrossRef]
22. Zavalikhin, D.V.; Frolov, V.A.; Fedorov, S.A. Experience and prospects for the development of equipment for light beam welding, brazing, and heat treatment (review). *Weld. Int.* **2009**, *23*, 856–860. [CrossRef]

23. Zhang, Y.; Chen, Y.; Yu, D.; Sun, D.; Li, H. A review paper on effect of the welding process of ceramics and metals. *Int. J. Mater. Prod. Technol.* **2020**, *9*, 16214–16236. [CrossRef]
24. Wang, Y.; Feng, J.; Zhang, L.; He, P.; Zhang, J. Microstructure of alumina ceramic/Ag–Cu–Ti brazing alloy/Kovar alloy joint. *Mater. Sci. Tech. Lond.* **2007**, *23*, 320–323. [CrossRef]
25. Ong, F.S.; Rheingans, B.; Goto, K.; Tobe, H.; Ohmura, T.; Janczak-Rusch, J.; Sato, E. Residual stress induced failure of Ti–6Al–4V/Si_3N_4 joints brazed with Ag-Cu-Ti filler: The effects of brazing zone's elasto–plasticity and ceramics' intrinsic properties. *J. Eur. Ceram. Soc.* **2021**, *41*, 6319–6329. [CrossRef]
26. Zhang, J.; Wang, G.; He, Y.a.; Sun, Y.; He, X. Effect of joining temperature and holding time on microstructure and shear strength of Ti_2AlC/Cu joints brazed using Ag–Cu filler alloy. *Mater. Sci. Eng. A* **2013**, *567*, 58–64. [CrossRef]
27. Wang, G.C.; Zhang, J.; Liu, X.W. Characterizing the Decomposition of Ti_2AlC during its Brazing with Cu by Using Ag–Cu Filler Alloy. In *Materials Science Forum*; Trans Tech Publications Ltd.: Kapellweg, Switzerland, 2013; Volume 762, pp. 607–611. [CrossRef]
28. Lu, C.; Wang, G.; Yang, G.; Fan, G.; Zhang, J.; Liu, X. Substitution behavior of Ag atoms in the Ti_2AlC ceramic. *J. Am. Ceram. Soc.* **2017**, *100*, 732–738. [CrossRef]
29. Gulina, L.B.; Tolstoy, V.P.; Kasatkin, I.A.; Fateev, S.A. Flower–like silver nanocrystals: Facile synthesis via a gas–solution interface technique. *J. Mater. Sci.* **2018**, *53*, 8161–8169. [CrossRef]
30. Yang, H.; Pei, Y.; Rao, J.; De Hosson, J.T.M. Self–healing performance of Ti_2AlC ceramic. *J. Mater. Chem.* **2012**, *22*, 8304–8313. [CrossRef]
31. Liu, P.; Xie, J.; Wang, A.; Ma, D.; Mao, Z. An interatomic potential for accurately describing the atomic–scale deformation behaviors of Ti_2AlC crystal. *Comp. Mater. Sci.* **2020**, *182*, 109757. [CrossRef]
32. Nicolaï, J.; Furgeaud, C.; Fonrose, B.W.; Bail, C.; Beaufort, M.F. Formation mechanisms of Ti_2AlC MAX phase on SiC–4H using magnetron sputtering and post–annealing. *Mater. Des.* **2018**, *144*, 209–213. [CrossRef]
33. Liao, T.; Wang, J.; Li, M.; Zhou, Y. First–principles study of oxygen incorporation and migration mechanisms in Ti_2AlC. *J. Mater. Res.* **2009**, *24*, 3190–3196. [CrossRef]
34. Liao, T.; Wang, J.; Zhou, Y. Ab initio modeling of the formation and migration of monovacancies in Ti_2AlC. *Scripta Mater.* **2008**, *59*, 854–857. [CrossRef]
35. Van der Walt, C.; Terblans, J.J.; Swart, H.C. Molecular dynamics study of the temperature dependence and surface orientation dependence of the calculated vacancy formation energies of Al, Ni, Cu, Pd, Ag, and Pt. *Comp. Mater. Sci.* **2014**, *83*, 70–77. [CrossRef]
36. Gao, Q.; Du, A.; Yang, Z. Structural inheritance and difference between Ti_2AlC, Ti_3AlC_2 and$Ti_5Al_2C_3$ under pressure from first principles. *Mod. Phys. Lett. B* **2017**, *31*, 1750016. [CrossRef]
37. Cao, L.; Wang, H.W.; Zou, C.M.; Wei, Z.J. Microstructural characterization and micromechanical properties of dual–phase carbide in arc–melted titanium aluminide base alloy with carbon addition. *J. Alloys Compd.* **2009**, *484*, 816–821. [CrossRef]
38. Tian, W.H.; Nemoto, M. Precipitation behavior of (Al, Ag)$_3$Ti and Ti_3AlC in L10–TiAl in Ti–Al–Ag system. *Intermetallics* **1999**, *7*, 1261–1269. [CrossRef]
39. Li, M.; Xiao, S.; Xu, L.; Tian, J.; Chen, Y. Microscale investigation of perovskite–Ti_3AlC strengthening and plastic deformation in high niobium containing TiAl alloys. *J. Alloys Compd.* **2021**, *857*, 157563. [CrossRef]